Robot-assisted superficial hyperthermia treatments: the ROBHOT system

Marco Ferro[1,*], Pierfrancesco Pavoni[2], Marilena Vendittelli[1]

***Abstract*— This paper presents the design, implemetation and experimental validation of the ROBHOT Technology Demonstrator, a new system for robot-assisted superficial hyperthermia treatments. The system features impedance-based interaction control for accurate and safe delivery of the treatment, a digital twin of the operative setup, communication modules with a pre-operative planning software. Results of the system validation in a relevant experimental environment are reported. A video clip presenting an overview of the system and the validation experiments is available at `https://youtu.be/rNxMaD-teNo`.**

I. INTRODUCTION

In oncology, hyperthermia (HT) is a treatment used to enhance chemotherapy (CT) and radiotherapy (RT) by improving complete response, local tumour control, and overall survival [1]. HT raises the temperature in tumour tissues to 40-45°C for about 60 minutes to: (i) inhibit tumour cell repair after RT, (ii) increase blood flow and re-oxygenation, enhancing RT sensitivity and CT delivery, and (iii) boost cell membrane permeability for better CT uptake. This temperature rise is achieved through absorption of an electromagnetic field radiated from one or multiple antennas. Superficial HT treats tumours up to 4-5 cm beneath the skin, with the antenna placed on the body surface at the tumour site.

Despite solid scientific foundation and clinical evidence [2]–[6], current procedures do not meet the level of accuracy, integration in the RT workflow, and procedural timing required to guarantee full exploitation of the treatment potential [7]–[10].Achieving quality requirements in tumours typically treated with superficial HT like, e.g., breast, head and neck, skin/extremities cancers, is challenging due to the varying size, morphology, and anatomical complexity of these tumours, which complicates antenna placement. Currently, RF antennas are manually positioned by a clinician using a passive mechanical arm without feedback on positioning. Once settled in position, the arm is fixed for the 60-minute treatment, making it difficult to reproduce the exact position in subsequent sessions and to track movements during treatment. Moreover, this manual process can degrade HT quality, irradiate healthy tissues, and result in longer procedural times and lower accuracy compared to RT standards.

*corresponding author

[1]The authors are with Department of Department of Computer, Control, and Management Engineering "Antonio Ruberti", Sapienza University of Rome, Via Ariosto 25, 00185, Rome, Italy. {ferro, vendittelli}@diag.uniroma1.it

[2] Medlogix Srl, Via Adriano Olivetti, 24, 00131 Rome, Italy, pf.pavoni@medlogix.eu

This work has been partially supported by the DIH HERO and the Sapienza Project RM120172AD69A503 "Development of innovative superficial hyperthermia applicators including automatic real-time adjustments for treatment optimization".

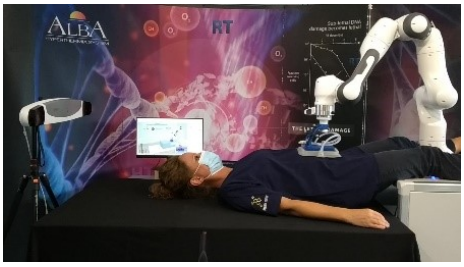

Fig. 1: The ROBHOT system: the superficial HT antenna is safely and accurately placed and kept in contact with the patient body, at the desired pose, by a Franka Emika PANDA manipulator integrating the information from the Polaris optical localization and tracking system and of a digital twin of the whole operating scenario.

We recently proposed the ROBHOT system[1] to address these challenges by integrating robotics into HT treatment. The system adopts a PANDA manipulator to safely position and maintain the antenna on the patient throughout the treatment, compensating for any patient movement (see Fig. 1). A Polaris optical tracking system ensures accurate registration of the pre-operative radiation plan. Data from the robot and optical sensor are combined in a digital twin, which includes a 3D model of the patient. To our knowledge, this is the first robotic superficial HT system ensuring accurate pre-operative plan registration and safe, comfortable antenna positioning from preparation to treatment. A related system [11] uses highly focused ultrasound, a different technology with similar therapeutic goals, but lacks a digital twin and controlled interaction force to ensure compliant robot behavior.

From a robotics perspective, key challenges to be solved include: i) registering the pre-operative plan in the robot's and optical camera's reference frames; ii) controlling physical human-robot interaction, occurring during manual guidance for initial positioning and throughout the treatment to maintain antenna contact with the patient.

The state-of-the-art in robot interaction control includes direct and indirect force control schemes: impedance/admittance control, force control, hybrid force/position control, and compliance control [12], widely used in various robotics fields. In medical robotics, the goal is to achieve autonomous or semi-autonomous behaviors for safe interaction with delicate anatomical structures, minimizing patient stress and pain [13]. In [14], a compliant comanipulation control architecture for robot-assisted medical procedures is presented, implementing both passive and active impedance control to manage dynamic interaction between the robot and a human operator. In [15], a method for controlling an ultrasound (US) probe manipulated by a robotic system regulates the interaction force with the target

[1]ROBHOT is a Technical Demonstrator with the financial support of the Digital Innovayion Hub HERO.

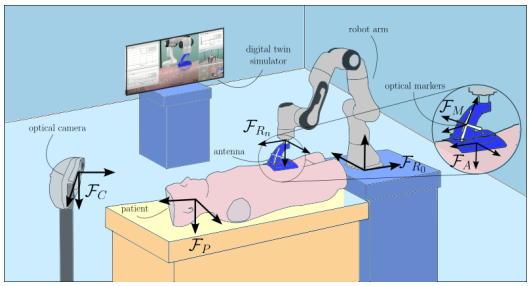

Fig. 2: Representation of the experimental setup.

(a) (b) (c)

Fig. 3: The NDI Polaris Vega system: (a) the optical camera; (b) the rigid-body frame with 4 optical markers, attached to the antenna for tracking; (c) the optical passive probe, used for registering the Polaris system to the environment.

surface while achieving visual control objectives based on acquired images. Impedance control schemes have also been used in beating-heart surgery [16], and a similar system architecture and interaction control have been proposed for robot-assisted ultrasound tissue scanning [17].

This work presents the design and validation of the ROBHOT Technology Demonstrator, a new treatment system with a software framework enabling seamless transition from simulation to experiments. This allows efficient movement from planning to treatment delivery. The system includes a digital twin, communication modules with pre-operative planning software, integration of various devices, and adaptability to different technology-assisted medical procedures.

ROBHOT features continuous physical interaction between the patient and medical devices at the robot's end-effector. The control approach allows easy manual guidance for initial positioning, quick removal from the operating field, and compliant interaction to accommodate patient movements, ensuring safety. The controllers are validated on the real system in an operational environment.

II. ROBHOT System Architecture

Robot assistance and full automation of superficial HT can match radiotherapy's accuracy and enhance patient safety and comfort. The ROBHOT demonstrator is crucial to this project, providing: (i) precise antenna positioning, (ii) visual monitoring via a digital twin with a 3D patient model, and (iii) ensured patient comfort and safety throughout treatment.

To achieve these objectives, the technological setup includes: (i) an NDI Polaris Vega optical camera with markers for real-time antenna tracking; (ii) a Franka Emika Panda robot for shared and autonomous antenna positioning; (iii) the CoppeliaSim software for 3D rendering and simulation; and (iv) dedicated software with layered architecture for communication and interaction among components, allowing integration of additional elements. Fig. 2 shows the components and reference frames: $\mathcal{F}_C$ (optical camera), $\mathcal{F}_{R_0}$ (robot base), $\mathcal{F}_{R_n}$ (robot tip), $\mathcal{F}_A$ (antenna), $\mathcal{F}_M$ (optical markers), and $\mathcal{F}_P$ (patient/target anatomy). The remainder of this Section provides technical details about these components.

A. NDI Polaris Vega ST optical camera

The NDI Polaris Vega ST in Fig. 3 is an optical system widely used in clinical settings for real-time pose tracking using near-infrared (IR) light technology. The system includes: i) a dedicated camera (Fig 3a), providing sub-millimeter accuracy (0.12 mm) at rates of 20, 30, or 60 Hz within a measurement volume, with latency under 16 ms; ii) a rigid-body frame with 4 passive optical markers (Fig 3b), for attaching to clinical instruments for tracking purposes; iii) a probe with 4 passive optical markers (Fig 3c), used for intra-operative patient registration, facilitating transfer of pre-operative plans to the robot; iv) API functions for system querying and custom application development.

In the ROBHOT system, a 4-marker rigid-body frame is mounted on the radiative antenna holder (Fig. 3b), for tracking pourposes. The passive probe enables intra-operative patient-Polaris registration (see Sect. III-A), while the API functions are integrated into a dedicated *proxy* class within the ROBHOT control software architecture (Sect. II-D).

B. Franka Emika PANDA robot manipulator

The Franka Emika PANDA (featured in Fig 1) is a fixed-base robot manipulator arm with 7 degrees of freedom, equipped with encoders and link-side torque sensors at each joint. The platform weight is around 18 kg, capable of holding payloads at the end-effector up to 3 kg, sufficient for standard radiative antennas and the water bolus needed for skin cooling in superficial hyperthermia treatments. The robot ensures positioning accuracy during motion of less than 1.25 mm, with force (torque) sensing resolution of < 0.05N (< 0.02Nm). A Franka Control Interface (FCI) allows low-level control at 1 kHz, while the open-source C++ library `libfranka` manages network communication and provides functionalities for reading robot state and sending commands from external applications. Commands can control position or velocity in Cartesian or joint space through the FCI's motion generator module. Alternatively, direct control of joint motors is possible by sending appropriate torque commands. These functionalities, including access to `libfranka`, are integrated into a dedicated *proxy* class within the ROBHOT software solution, detailed in Sect. II-D.

C. CoppeliaSim simulation software

CoppeliaSim (formerly V-REP) is a simulation software offering a versatile environment for robot motion planning and control, and supporting multi-robot applications in various programming languages (C/C++, Python, Java, Lua, Matlab, Octave) and deployment solutions (embedded plugin, ROS node, external remote API client). The high degree of customization of the virtual scenes is ideal for creating the *digital twin* of our system, i.e., an enhanced virtual reconstruction of the operational environment with advanced visualization and signal monitoring capabilities. In the ROBHOT system, CoppeliaSim's remote API functions connect the simulator with the robot and optical camera,

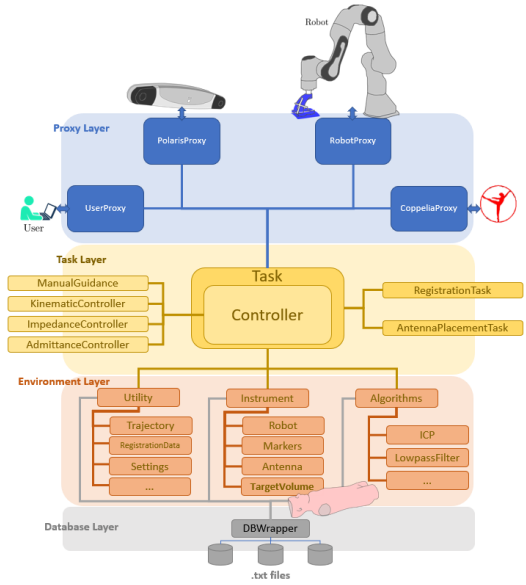

Fig. 4: Flowchart of the multi-layer ROBHOT software architecture. The software manages the communication with the involved external systems, the execution of the treatment routines, the control of the robot and the update of th environment state.

integrated into a dedicated proxy class within our software architecture (see Sect.Sect. II-D).

D. Software architecture

The multi-layer ROBHOT software architecture is shown in Fig. **??**, slightly modified from [18].

The top layer (blue box) interfaces external systems with lower-level functionalities through *proxy* objects using dedicated libraries and SDKs. Integrated systems include the Franka robot, Polaris optical camera, CoppeliaSim simulator, and a user interface. This component validates interaction control strategies in simulation and demonstrates flexibility for future remote operation extensions.

The middle layer (yellow box) runs high-level routines, coordinating data from proxies to update the environment state stored in the lower levels. This includes tasks like registration, antenna tracking, and robot-assisted placement, or implementing and comparing various control strategies.

The lower layer (red box) represents fundamental components, such as the robot, antenna, and target volume, and includes mathematical tools like algorithms and filters. These objects handle tasks such as updating the robot's state or executing registration algorithms. File system operations for each component are managed in the final layer (gray box).

Proxies, task objects, and controller objects use dedicated threads. Proxies periodically update data from external systems and share it with task-level routines. Task and controller threads retrieve this data, execute routines, and interact with the environment's state at the lower level. A video clip of the ROBHOT Digital Twin is available at `https://youtu.be/d-_I7URcdVc`.

III. HYPERTHERMIA TREATMENT AUTOMATION

Integrating the NDI Polaris optical camera and the Franka Emika Panda manipulator into the clinical setting enables the treatment procedure with *assisted* manual antenna positioning, facilitated by real-time antenna tracking using the optical camera. Moreover, it provides the capability for *autonomous* or *semi-autonomous* antenna positioning. Leveraging the robot's high accuracy and repeatability, it controls the antenna's pose and can actively adjust to unintended physiological patient movements, such as breathing.

In both treatment modalities, the setup incorporates a *digital twin* of the clinical scenario within the CoppeliaSim environment. This includes a 3D model of the anatomical region of interest, reconstructed from CT scans obtained during the pre-operative phase. These scans are available from the pre-operative phase of the treatment and are used by clinicians to plan the antenna's desired location, ensuring the target tumour remains within the maximum Specific Absorption Rate (SAR) volume of the antenna.

In the pre-operative planning phase of hyperthermia treatment, the desired antenna pose is determined relative to the patient's reference frame. To accurately assess positioning accuracy, it's essential to align the treatment plan with the robot and camera reference frames. Therefore, we implemented a registration procedure using *fiducial* markers to estimate the relative camera-patient and robot-patient spatial relationships. In the following sections, we will outline the registration procedures for both the camera and robot systems. Subsequently, we will describe the optical-based and robot-based treatment modalities provided by ROBHOT.

A. Registration

Referring to the frames specified in Fig. 2, the marker-based registration procedure estimates the 4×4 homogeneous transformation matrices ${}^{P}\boldsymbol{T}_{C}$ and ${}^{P}\boldsymbol{T}_{R_0}$, denoting the relative pose of the robot and camera frames $\mathcal{F}_{R_0}$ and $\mathcal{F}_{C}$ with respect to the patient frame $\mathcal{F}_{P}$, respectively.

Four radiopaque markers are initially placed on the target anatomy for visibility in CT scans, allowing direct measurement of their coordinates ${}^{P}\boldsymbol{p}_i \in \mathcal{F}_P$, where $i = 1, \ldots, 4$. To achieve accurate marker-based registration, coordinates of these points in the respective reference frames to be registered ${}^{X}\boldsymbol{p}_i$ (where $X = \{C, R_0\}$) must be acquired. An Iterative Closest Point (ICP) algorithm [19] is then applied to these coordinate sets to estimate the transformations between the frames. Depending on the system being registered (camera or robot), the corresponding set of coordinates is obtained using different methods.

1) Optical camera registration: the coordinates ${}^{C}\boldsymbol{p}_i \in \mathcal{F}_C$ are manually acquired by the operator using the NDI passive probe (see Fig. 3c), which touches the fiducial markers. The ICP algorithm then leverages the acquired coordinates sets ${}^{C}\boldsymbol{p}_i$ and ${}^{P}\boldsymbol{p}_i$ to compute the transformation ${}^{P}\boldsymbol{T}_{C}$. An example of the operator moving the robot to acquire these points and the resulting estimated transformation applied in the simulated environment is shown in Fig. 5. The final experimental reprojection error of the estimated transformation was approximately $4 \cdot 10^{-3}$ m.

2) Robot registration: The coordinates ${}^{R}\boldsymbol{p}_i \in \mathcal{F}_{R_0}$ of points on the target anatomy are measured using the Franka robot gripper. The built-in manual guidance control mode provided

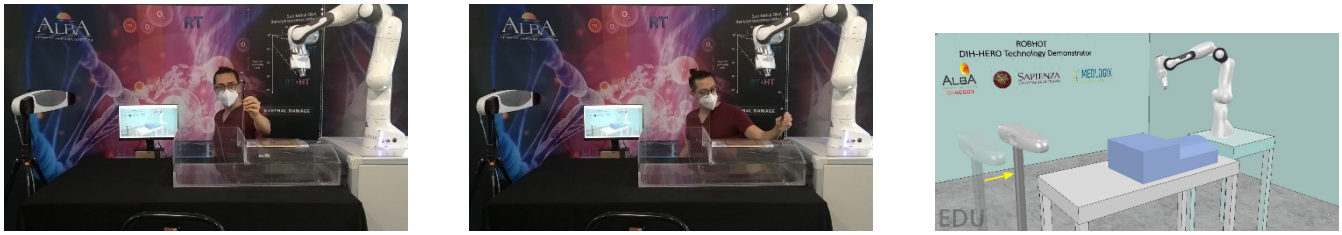

(a) (b) (c)

Fig. 5: Registration of the "patient" (transparent phantom on the table between the camera and the robot) with respect to the optical camera system. The user handles the optical passive probe to acquire the points of interest in the reference frame of the camera.

(a) (b) (c)

Fig. 6: Registration of the "patient" (transparent phantom on the table between the camera and the robot) with respect to the robot system. The user exploits the manual guidance functionalities of the designed system to manipulate the robot end-effector and place its tip in correspondance with the points of interest in the reference frame of the robot.

by the `libfranka` library allows the user to move the gripper and position the tip over the fiducial markers. The ICP algorithm then leverages the acquired coordinates sets ${}^{R_0}\boldsymbol{p}_i$ and ${}^{P}\boldsymbol{p}_i$ to compute the transformation ${}^{P}\boldsymbol{T}_{R_0}$. An example of the operator moving the robot to acquire these points and the resulting estimated transformation applied in the simulated environment is illustrated in Fig. 6. In our experimental validation, the final reprojection error of the estimated transformation was approximately $2.07 \cdot 10^{-4}$ m.

Once ${}^{P}\boldsymbol{T}_{R_0}$ and ${}^{P}\boldsymbol{T}_{C}$ are known, it is possible to transfer geometric information from the robot to the camera frame and vice-versa, by computing the corresponding transformation: ${}^{R_0}\boldsymbol{T}_{C} = {}^{P}\boldsymbol{T}_{R}^{-1}\,{}^{P}\boldsymbol{T}_{C}$. While this transformation can be obtained through a camera-robot calibration procedure, the patient-camera and patient-robot registrations is however a useful system functionality, enabling also manual or robot-assisted treatment delivery in an exclusive way.

B. Antenna reference pose determination

The reference pose of the radiative antenna frame $\mathcal{F}_{A,r}$ is determined by a treatment planner using available medical images (e.g., CT scans) to simulate antenna radiation on the target anatomy. This simulation identifies the reference pose ${}^{P}\boldsymbol{T}_{A,r}$, specifying antenna's position and orientation in the patient frame $\mathcal{F}_P$, maximizing coverage within the antenna SAR region for proper positioning during treatment delivery.

When a planning system is unavailable, ROBHOT also employs an alternative method based on operator experience. This method involves using a template sheet placed over the target surface, detailing the antenna size and nominal SAR area. The operator then uses a passive probe tool to acquire a set of 6 reference points ${}^{C}\boldsymbol{p}_i$, $i = 1, \ldots, 6$, in the camera frame $\mathcal{F}_C$ along the perimeter of the antenna marked on the sheet. Subsequently, similar to the optical camera registration routine, the ICP algorithm is employed to compute the corresponding reference pose ${}^{C}\boldsymbol{T}_{A,r}$ of the antenna that best matches the measured points.

C. Intra-operative treatment delivery workflow

Once the antenna reference pose $\mathcal{F}_{A,r}$ is determined, the ROBHOT software loads into the virtual environment: i) the 3D model of the patient's target anatomy, characterized by the frame $\mathcal{F}_P$; ii) the transformation matrices ${}^{P}\boldsymbol{T}_{C}$ and ${}^{P}\boldsymbol{T}_{R}$ for the optical camera and robot base; iii) the antenna reference pose ${}^{P}\boldsymbol{T}_{A,r}$ or ${}^{C}\boldsymbol{T}_{A,r}$.

To guide the antenna to the reference pose and ensure safe contact with the patient for effective treatment, the ROBHOT system employs three operational modes. These modes can be used alternatively or complementarily:

1) ***Manual guidance***: the operator manipulates the radiative antenna by applying forces, such as pushing or pulling, directly to the robot manipulator arm. The robot pose is tracked and visualised in the virtual environment;

2) ***Autonomous antenna reference pose regulation***: the antenna's initial pose ${}^{R}\boldsymbol{T}_{A,i}$ is adjusted to an intermediate *proxy* pose ${}^{R}\boldsymbol{T}_{A,p}$, by shifting the reference ${}^{R}\boldsymbol{T}_{A,r}$ along the vertical axis of $\mathcal{F}_A$ (blue axis in Fig. 7) to avoid contact with the patient. It can follow a previous *manual guidance* mode to achieve finer adjustments, or operate independently, guiding the antenna from any initial configuration.

3) ***Autonomous interaction control***: following the *Autonomous antenna reference pose regulation* mode, this phase manages the approach of the antenna to the patient's anatomy to achieve controlled contact.

IV. Robot control

Autonomous placement of the radiative antenna must control the prolonged contact between the antenna and the patient. In particular, the control system must ensure: i) stable

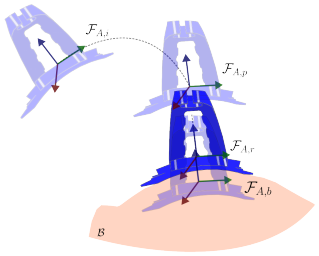

Fig. 7: Regulation of the antenna to the reference pose through a preliminary motion to the *proxy* pose $\mathcal{F}_{A,p}$ of the antenna frame.

(a) (b) (c)

Fig. 8: External view of the different phases of the robot-assisted antenna positioning procedure: (a) approaching; (b) achieving contact; (c) breathing adaptation based on impedance control.

interaction with limited force, and ii) reactive behavior to accommodate patient movements.

Additionally, considering compatibility and legal approvals of novel systems in clinical environments, we designed the system with a minimum number of additional devices, excluding a dedicated F/T sensor at the robot end-effector. Notwithstanding, we highlight that joint torque sensors and the robot's dynamic model still allow estimation of interaction forces through momentum-based observers [20].

An *impedance* control scheme suits our setup, modeling the patient body as a mechanical system with finite stiffness. This scheme indirectly controls interaction force by regulating a Cartesian pose error, with control gains tuned to achieve desired interaction dynamics, while it can achieve indirect force regulation without using direct force measurements.

In details, the design of an impedance control scheme exploits the knowledge of the robot dynamic model

$$\boldsymbol{M}(\boldsymbol{q})\ddot{\boldsymbol{q}} + \boldsymbol{C}(\boldsymbol{q},\dot{\boldsymbol{q}})\dot{\boldsymbol{q}} + \boldsymbol{g}(\boldsymbol{q}) + \boldsymbol{\tau}_f = \boldsymbol{\tau} + \boldsymbol{J}(\boldsymbol{q})^T\boldsymbol{F}_{ext}, \quad (1)$$

where $\boldsymbol{M}(\boldsymbol{q}) \in \mathbb{R}^{n\times n}$ is the inertia matrix, $\boldsymbol{C}(\boldsymbol{q},\dot{\boldsymbol{q}}) \in \mathbb{R}^{n\times n}$ is the matrix of Coriolis and centrifugal forces, $\boldsymbol{g}(\boldsymbol{q}) \in \mathbb{R}^n$ is the gravity vector and $\boldsymbol{\tau}_f \in \mathbb{R}^n$ the friction torques.

Typically, the interaction between the robot and the environment is modeled as a linear mass-spring-damper system:

$$\boldsymbol{M}_m\boldsymbol{\Delta}\ddot{\boldsymbol{x}} + \boldsymbol{D}_m\boldsymbol{\Delta}\dot{\boldsymbol{x}} + \boldsymbol{K}_m\boldsymbol{\Delta}\boldsymbol{x} = \boldsymbol{F}_{ext} \quad (2)$$

where $\boldsymbol{M}_m$, $\boldsymbol{D}_m$ and $\boldsymbol{K}_m$ are desired inertia, damping and stiffness matrices, respectively, while $\boldsymbol{\Delta x} = \boldsymbol{x} - \boldsymbol{x}_d$ denotes the error of the robot end-effector pose $\boldsymbol{x}$ with respect to the desired reference $\boldsymbol{x}_d$.

However, denoting by $\boldsymbol{M}_{\boldsymbol{x}}(\boldsymbol{q})$ the robot Cartesian inertia matrix, it is also possible to shape the desired interaction as a nonlinear configuration-dependent model. This is obtained by choosing $\boldsymbol{M}_m = \boldsymbol{M}_{\boldsymbol{x}}(\boldsymbol{q})$ and adding a Coriolis/centrifugal term to the damping term to preserve physical feasibility. In this case, the torque control input $\boldsymbol{\tau}$ is given by

$$\boldsymbol{\tau} = \boldsymbol{M}\boldsymbol{J}^{\#}\left(\ddot{\boldsymbol{x}}_d - \dot{\boldsymbol{J}}\boldsymbol{J}^{\#}\dot{\boldsymbol{x}}_d\right) + \boldsymbol{C}\boldsymbol{J}^{\#}\dot{\boldsymbol{x}}_d + \boldsymbol{g} + \boldsymbol{J}^T\boldsymbol{u}_{PD}, \quad (3)$$

where $\boldsymbol{u}_{PD} = (\boldsymbol{D}_m\boldsymbol{\Delta}\dot{\boldsymbol{x}} + \boldsymbol{K}_m\boldsymbol{\Delta}\boldsymbol{x})$. Indeed, this results in the following desired interaction model

$$\boldsymbol{M}_{\boldsymbol{x}}(\boldsymbol{q})\boldsymbol{\Delta}\ddot{\boldsymbol{x}} + (\boldsymbol{D}_m + \boldsymbol{C}_{\boldsymbol{x}}(\boldsymbol{q},\dot{\boldsymbol{q}}))\,\boldsymbol{\Delta}\dot{\boldsymbol{x}} + \boldsymbol{K}_m\boldsymbol{\Delta}\boldsymbol{x} = \boldsymbol{F}_{ext}. \quad (4)$$

The closed-loop system's dynamic response from the control law (3) depends on the impedance gains $\boldsymbol{D}_m$ and $\boldsymbol{K}_m$. This desired impedance model keeps contact forces limited while ensuring desired stiffness/compliance dynamics.

In the considered scheme, the interaction force arises from the antenna's reference pose being intentionally placed slightly inside the environment, driving the antenna towards the body surface to produce the intended collision. The reference pose displacement also affects the interaction force magnitude, adding another design parameter for shaping the impedance model. Details of the validation are in Section V.

V. Experimental Results

This section details the experimental validation of interaction control in a simulated robot-assisted hyperthermia treatment on a healthy subject. A predefined antenna reference pose ${}^R\boldsymbol{T}_{A,r}$ in $\mathcal{F}_R$ is selected to place it in contact with the subject's chest (see Fig. 8), defining the proxy pose ${}^R\boldsymbol{T}_{A,p}$ and the body reference pose ${}^R\boldsymbol{T}_{A,b}$, a few centimeters below the reference pose along the antenna z-axis.

The experiment began with "***Autonomous antenna reference pose regulation***", where the robot autonomously drives the antenna towards the reference pose (see Fig. 8a). A trajectory with a linear Cartesian path between the initial antenna pose ${}^R\boldsymbol{T}_{A,i}$ and the *proxy* reference pose ${}^R\boldsymbol{T}_{A,p}$ was generated, using a bang-coast-bang acceleration profile. The trajectory enables the antenna to accelerate to $v_{max} = 0.2[m/s]$ and $a_{max} = 0.25[m/s^2]$, maintain constant velocity, and decelerate for precise alignment. The impedance control law (3) with $\boldsymbol{K}_m = \text{diag}(3\cdot10^3, 3\cdot10^3, 3\cdot10^3, 2\cdot10^2, 2\cdot10^2, 2\cdot10^2)$ and $\boldsymbol{D}_m = \text{diag}(5\cdot10, 5\cdot10, 5\cdot10, 5, 5, 5)$ ensured a *stiff* dynamic behavior. The tracking performance is shown in the blue-colored range of plots in Fig. 9-10.

Upon reaching the antenna *proxy* pose ${}^R\boldsymbol{T}_{A,p}$, the system switched to "***Autonomous interaction control***" mode. Here, the autonomous control targeted the *body* reference pose ${}^R\boldsymbol{T}_{A,b}$ with a linear Cartesian path. The control strategy was designed to be *stiff* along planar x and y axes for position and vertical z axis for orientation, and *compliant* along z axis for position and x and y axes for orientation. This ensured the antenna adapted to the patient's movements while maintaining precise control. The effectiveness of this strategy is shown in the green and red-colored ranges of plots in Fig. 9- 10, with the vertical dashed line at $t = 7.5$s marking the transition to interaction control phase.

Finally, Fig. 11 shows the interaction forces and torques of the antenna with the subject's chest (see Fig.8c). Peak force values can be modified through impedance model

parameters, while oscillatory behavior can be reduced with a feedforward action compensating for breathing. Future work will include real-time tracking of the body area. A video clip of the experiments is available at `https://youtu.be/rNxMaD-teNo`.

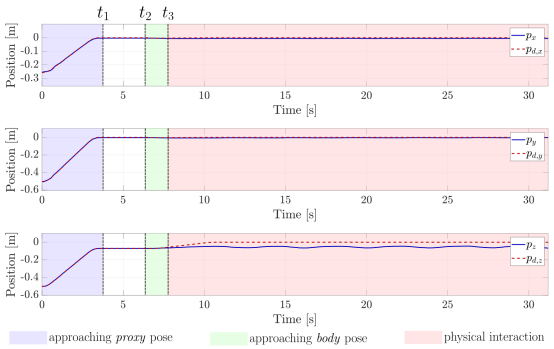

Fig. 9: Position tracking performance: autonomous regulation of the antenna to the *proxy* pose ${}^{R}\boldsymbol{T}_{A,p}$ (shaded blue), achieved at $t_1 = 3.5$s; autonomous regulation to the *body* pose ${}^{R}\boldsymbol{T}_{A,b}$ (shaded green), starting at $t_2 = 6.5$s; physical interaction phase (shaded red) from the antenna contacting the subject's chest at $t_3 = 7.5$s. The target pose is intentionally set within the body, making it unreachable by the antenna.

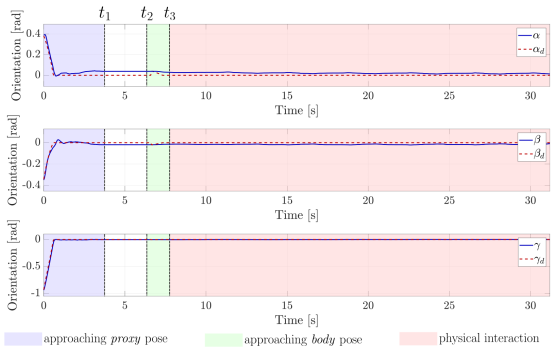

Fig. 10: Orientation tracking during the physical interaction between the antenna and the human subject. Time instants t_1, t_2 and t_3 and the shaded area as in Fig. 9.

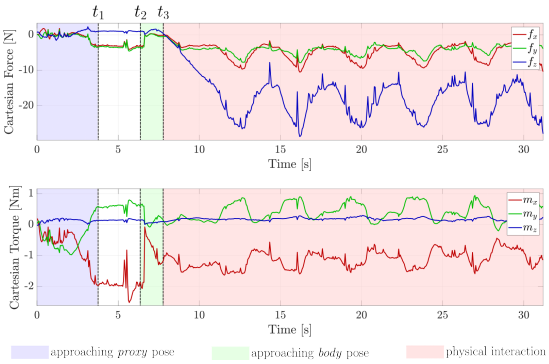

Fig. 11: Cartesian forces resulting from the physical interaction between the antenna and the human subject. Time instants t_1, t_2 and t_3 and the shaded area as in Fig. 9.

VI. Conclusions

The paper presented a robot-assisted superficial hyperthermia system allowing to achieve unprecedent accuracy while guaranteeing safety. Future work includes tracking of human motion, to reduce the oscillation in the interaction force, and a non-invasive internal temperature estimation using the method in [21] and [22].

References

[1] N. R. Datta, E. Puric, D. Klingbiel, S. Gomez, and S. Bodis, "Hyperthermia and radiation therapy in locoregional recurrent breast cancers: A systematic review and meta-analysis," *Int. Journal of Radiation Oncology*Biology*Physics*, vol. 94, no. 5, pp. 1073–1087, 2016.

[2] P. B. Elming, B. S. Sørensen, *et al.*, "Hyperthermia: The optimal treatment to overcome radiation resistant hypoxia," *Cancers*, 2019.

[3] M. Hurwitz and P. Stauffer, "Hyperthermia, radiation and chemotherapy: The role of heat in multidisciplinary cancer care," *Seminars in Oncology*, vol. 41, no. 6, pp. 714–729, 2014.

[4] W. C. Dewey, L. E. Hopwood, S. A. Sapareto, and L. E. Gerweck, "Cellular responses to combinations of hyperthermia and radiation," *Radiology*, vol. 123, no. 2, pp. 463–474, 1977.

[5] B. Hildebrandt, P. Wust, O. Ahlers, A. Dieing, G. Sreenivasa, T. Kerner, R. Felix, and H. Riess, "The cellular and molecular basis of hyperthermia," *Critical Reviews in Oncology/Hematology*, vol. 43, no. 1, pp. 33–56, 2002.

[6] A. Oei, L. Vriend, J. Crezee, *et al.*, "Effects of hyperthermia on dna repair pathways: one treatment to inhibit them all," *Radiat Oncol*, vol. 10, no. 165, 2015.

[7] C. van Leeuwen, A. Oei, K. Chin, H. Crezee, A. Bel, A. Westermann, M. Buist, N. Franken, L. Stalpers, and H. Kok, "A short time interval between radiotherapy and hyperthermia reduces in-field recurrence and mortality in women with advanced cervical cancer," *Radiation Oncology*, vol. 12, 04 2017.

[8] H. Crezee, H. P. Kok, A. L. Oei, N. A. P. Franken, and L. J. A. Stalpers, "The impact of the time interval between radiation and hyperthermia on clinical outcome in patients with locally advanced cervical cancer," *Frontiers in Oncology*, vol. 9, 2019.

[9] A. Bakker, J. van der Zee, G. van Tienhoven, H. P. Kok, C. R. N. Rasch, and H. Crezee, "Temperature and thermal dose during radiotherapy and hyperthermia for recurrent breast cancer are related to clinical outcome and thermal toxicity: a systematic review," *International Journal of Hyperthermia*, vol. 36, no. 1, pp. 1023–1038, 2019.

[10] M. D. Greef, H. P. Kok, A. Bel, and J. Crezee, "3d versus 2d steering in patient anatomies: A comparison using hyperthermia treatment planning," *Int. J. of Hyperthermia*, vol. 27, no. 1, pp. 74–85, 2011.

[11] A. Mariani, L. Morchi, A. Diodato, S. Tognarelli, and A. Menciassi, "High-intensity focused ultrasound surgery based on kuka robot: A computer-assisted platform for noninvasive surgical treatments on static and moving organs," *IEEE Robotics Automation Magazine*, vol. 30, no. 3, pp. 79–93, 2023.

[12] B. Siciliano and O. Khatib, *Springer Handbook of Robotics*, 2016.

[13] T. Haidegger, B. Benyó, L. Kovács, and Z. Benyó, "Force sensing and force control for surgical robots," *IFAC Proceedings Volumes*, vol. 42, no. 12, pp. 401–406, 2009.

[14] C. Sousa, R. Cortesao, and P. Queiros, "Compliant comanipulation control for medical robotics," in *2009 2nd Conference on Human System Interactions*, 2009, pp. 265–271.

[15] P. Chatelain, A. Krupa, and N. Navab, "Confidence-driven control of an ultrasound probe," *IEEE Transactions on Robotics*, vol. 33, no. 6, pp. 1410–1424, 2017.

[16] L. Cheng and M. Tavakoli, "Ultrasound image guidance and robot impedance control for beating-heart surgery," *Control Engineering Practice*, vol. 81, pp. 9–17, 2018.

[17] M. Dyck, A. Weld, J. Klodmann, *et al.*, "Toward safe and collaborative robotic ultrasound tissue scanning in neurosurgery," *IEEE Transactions on Medical Robotics and Bionics*, vol. 6, no. 1, pp. 64–67, 2024.

[18] M. Ferro, C. Gaz, M. Anzidei, and M. Vendittelli, "Online needle-tissue interaction model identification for force feedback enhancement in robot-assisted interventional procedures," *IEEE Transactions on Medical Robotics and Bionics*, vol. 3, no. 4, pp. 936–947, 2021.

[19] P. Besl and N. D. McKay, "A method for registration of 3-d shapes," *IEEE Transactions on Pattern Analysis and Machine Intelligence*, vol. 14, no. 2, pp. 239–256, 1992.

[20] S. Haddadin, A. De Luca, and A. Albu-Schäffer, "Robot collisions: A survey on detection, isolation, and identification," *IEEE Transactions on Robotics*, vol. 33, no. 6, pp. 1292–1312, 2017.

[21] A. Cristofaro, G. Cappellini, E. Staffetti, G. Trappolini, and M. Vendittelli, "Adaptive estimation of the pennes' bio-heat equation - i: Observer design," in *2023 62nd IEEE Conf. on Decision and Control (CDC)*, 2023, pp. 1931–1936.

[22] G. Cappellini, G. Trappolini, E. Staffetti, A. Cristofaro, and M. Vendittelli, "Adaptive estimation of the pennes' bio-heat equation - ii: A nn-based implementation for real-time applications," in *2023 62nd IEEE Conf on Decision and Control (CDC)*, 2023, pp. 5364–5369.